



**HAL**  
open science

## Signal analysis and identification for induction motor sensorless control

Lotfi Baghli, I. Al-Rouh, A. Rezzoug

► **To cite this version:**

Lotfi Baghli, I. Al-Rouh, A. Rezzoug. Signal analysis and identification for induction motor sensorless control. *Control Engineering Practice*, 2006, 14 (11), pp.1313-1324. 10.1016/j.conengprac.2005.06.016 . hal-03562592

**HAL Id: hal-03562592**

**<https://hal.univ-lorraine.fr/hal-03562592>**

Submitted on 9 Feb 2022

**HAL** is a multi-disciplinary open access archive for the deposit and dissemination of scientific research documents, whether they are published or not. The documents may come from teaching and research institutions in France or abroad, or from public or private research centers.

L'archive ouverte pluridisciplinaire **HAL**, est destinée au dépôt et à la diffusion de documents scientifiques de niveau recherche, publiés ou non, émanant des établissements d'enseignement et de recherche français ou étrangers, des laboratoires publics ou privés.

# Signal Analysis and Identification for Induction Motor Sensorless Control

L. Baghli \*, I. Al-Rouh, and A. Rezzoug  
 Groupe de Recherche en Electrotechnique et Electronique de Nancy  
 GREEN-UHP, CNRS UMR – 7037  
 Université H. Poincaré, BP 239, 54506 Vandœuvre-lès-Nancy

---

## Abstract

This paper presents signal analysis and identification methods for achieving sensorless vector control of induction motors. The sensorless scheme is based on high frequency signal injection for operating at low and zero speed. The identification is done using least square algorithm and sliding discrete Fourier transform. Analog and digital filtering problems are also discussed. Simulation and experimental results are presented to confirm theoretical studies.

**Keywords:** Identification; induction machine; high frequency signal injection; saliencies; filtering; sliding discrete Fourier transform; speed estimation; sensorless control.

---

## 1. Introduction

Even if sensorless induction machine control theory and application are not new, intensive research is still carried out on the subject. Nominal and high speed operation give satisfactory results. However, problems lie in low speed region and in position control (Holtz, 1998, 2002).

Many works use high frequency signal injection to make the system observable independently from fundamental excitation.

These schemes are based on the presence of saliencies or anisotropies. Depending on the tracking target (stator flux or rotor position), different processing schemes exist. Rotor and stator configurations (like slot number and slot opening (Degner and Lorenz, 1997 and Wolbank et al. 2003)) are critical parameters that give more or less interesting results in terms of signal to noise ratio and thus, of implementation feasibility and control robustness.

To track rotor position, we need the strong presence of an anisotropy that is linked to the rotor and we would like to lower the anisotropy that is due to saturation. Indeed, saturation will disturb the estimation and we must try to compensate its effects (Teske et al. 2000a).

On the other hand, if we want to estimate the field

angle, we will necessarily look for the second type of anisotropy or saliency while trying to compensate rotor slots and custom engineered saliency effects.

Research is also carried towards carrier injection methods. Revolving or alternating carrier methods (Degner and Lorenz (1997), Teske et al. (2000a), Jansen (1993), Ha and Sul (1997)) have the advantage of allowing frequency domain analysis. Whereas burst injection (Staines et al., 1999), INFORM method (Schroedl, 1996 and Wolbank et al. 2003) or PWM natural switching require signal processing using time-domain methods. Current injection methods with current fed induction motor (CRPWM) can also be used to obtain sensorless vector control (Blaschke et al. 1996). There are also methods based on zero sequence air gap flux detection (Consoli and Testa, 2003).

In this work, we will use a revolving carrier excitation method. We will focus on the identification of the carrier components of the current by means of a least square algorithm (LSA) and thanks to an original application of sliding discrete Fourier transform (SDFT) filtering.

We will discuss filtering problems because of their great importance in sensorless control schemes (Teske et al. 2000a) where information signal is of very low magnitude in respect to the fundamental one. We will point out at the closed loop difficulties in sensorless field oriented control with or without speed control loop.

---

\* Corresponding author: Lotfi BAGHLI, Tel: +33 3836 84132; fax: +33 3836 84133; e-mail: lotfi.baghli@green.uhp-nancy.fr.

## 2. Theory of Saliencies

The theory has already been presented in Holtz (2002), Degner and Lorenz (1997) and Jansen (1993). So we will merely introduce the current components and, by the way, we will establish the symbols used in this paper.

A saliency that is linked to the rotor can be represented in a high frequency model thanks to a leakage inductance tensor. In a reference frame that rotates at  $\frac{h}{2}\dot{\theta}_r$ , and with "d" axis aligned with the most saturated part, we obtain a diagonal tensor. In stator reference frame, this tensor becomes:

$$L_{\sigma s}^s = \begin{bmatrix} \sum L_{\sigma s}^e + \Delta L_{\sigma s}^e \cos(h\theta_r) & \Delta L_{\sigma s}^e \sin(h\theta_r) \\ \Delta L_{\sigma s}^e \sin(h\theta_r) & \sum L_{\sigma s}^e - \Delta L_{\sigma s}^e \cos(h\theta_r) \end{bmatrix} \quad (1)$$

Where  $\sum L_{\sigma s}^e$  and  $\Delta L_{\sigma s}^e$  are, respectively, the mean and the difference between  $d$  and  $q$  axis total leakage inductances in the saliency reference frame.  $h$  is the rank of the space harmonic of the saliency and must be even but it can be negative, positive or null.  $\theta_r$  is the rotor position.

Through a voltage fed inverter (VFI), we feed the stator with additional symmetrical carrier voltage (Fig. 1). The machine reaction to the high frequency excitation is acquired through current measurement. Then, signal processing is done thanks to special algorithms to extract the motor speed.

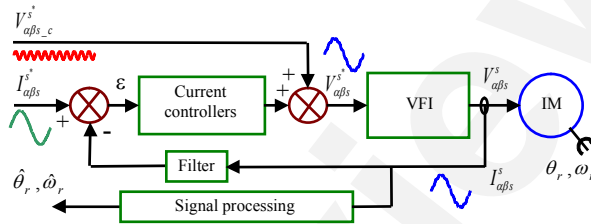


Fig. 1. Control and signal processing scheme.

In the case of only one saliency, the corresponding current component is:

$$I_{\alpha\beta s-c}^s = \frac{V_c}{\omega_c} \frac{\sum L_{\sigma s}^e}{\sum L_{\sigma s}^{e2} - \Delta L_{\sigma s}^{e2}} \begin{bmatrix} \cos\left(\omega_c t - \frac{\pi}{2}\right) \\ \sin\left(\omega_c t - \frac{\pi}{2}\right) \end{bmatrix} + \frac{V_c}{\omega_c} \frac{\Delta L_{\sigma s}^e}{\sum L_{\sigma s}^{e2} - \Delta L_{\sigma s}^{e2}} \begin{bmatrix} \cos\left(h\theta_r - \omega_c t + \frac{\pi}{2}\right) \\ \sin\left(h\theta_r - \omega_c t + \frac{\pi}{2}\right) \end{bmatrix} \quad (2)$$

It can be rewritten using the complex representation of space vectors (Holtz, 2002):

$$I_{\alpha\beta s-c}^s = I_{cp} e^{j\left(\omega_c t - \frac{\pi}{2} + \varphi_{cp}\right)} + I_{cn} e^{j\left(h\theta_r - \omega_c t + \frac{\pi}{2} + \varphi\right)} \quad (3)$$

The upper script  $s$  denotes the stator reference frame, while the subscripts  $\alpha\beta s$  indicate the stator complex representation. The last subscript  $_c$  shows the component due only to the injected carrier of angular frequency  $\omega_c$ .

Fig. 2 represents these vectors as well as the carrier voltage vector in a stator reference frame. The vector rotation direction is also reported, showing the positive and negative sequence type. The magnitude of the positive sequence current is actually much higher than that of the negative sequence. Therefore, it is difficult to extract the negative sequence signal, which is the only component holding the information.

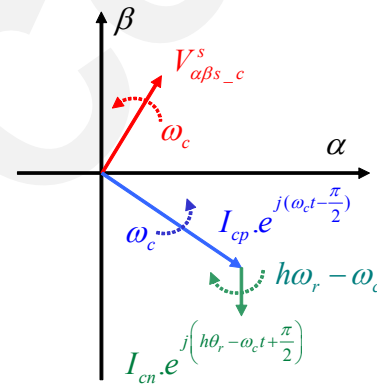


Fig. 2. Stator voltage and currents components vector with respect to their rotation speed in a saliency case.

With multiple saliencies, we will obtain the sum of multiple current components:

$$I_{\alpha\beta s-c}^s = I_{cp} e^{j\left(\omega_c t - \frac{\pi}{2} + \varphi_{cp}\right)} + \sum_i I_{cni} e^{j\left(h_i \theta_r - \omega_c t + \frac{\pi}{2} + \varphi_i\right)} \quad (4)$$

$h_i$  is the harmonic number of the  $i^{th}$  saliency configuration. The additional phase takes into account filtering lag and position of the saliency in respect of the rotor.

In the  $-\omega_c$  reference frame, the negative sequence components (due to the signal injection) are given by:

$$I_{\alpha\beta s-cn}^{-\omega_c} = \sum_i I_{cni} e^{j\left(h_i \theta_r + \frac{\pi}{2} + \varphi_i\right)} \quad (5)$$

In fact, many negative sequence components can be found as a consequence of the carrier injection (Holtz, 2002):

- The components of frequency  $-\omega_c + h_i \omega_r$  (with  $\omega_r$  the rotor electrical speed), are the ones that

interest us because they are directly linked to the rotor engineered saliency. Unfortunately, these components are of very low magnitude and require special care to separate them from the other current components. Let us note that, with multiple saliencies, we will get multiple terms and frequency components related to each  $h_i$ . We will then focus on the dominant engineered saliency in order to extract rotor position and speed.

- The components of frequency  $-\omega_c + h_i \omega_s$ , for our application, are disturbing components that are linked to the main flux. Their magnitude is a function of main flux saturation and load (Degner and Lorenz, 1997). These components share the same frequency intervals as the  $-\omega_c + h_i \omega_r$  one and make extracting and filtering difficult (Teske et al. 2000a).
- The component of frequency  $-\omega_c$  : is mainly due to winding asymmetries or offsets in current ( $\alpha\beta$ ) measurements. This component is of a fixed frequency but, when the speed becomes null, the  $-\omega_c + h_i \omega_r$  component will move across the  $-\omega_c$  one. So, this disturbing component has to be commissioned.
- The component of frequency  $-\omega_c + \frac{N_r}{p} \omega_r$  is due to rotor slots ( $N_r$ ). This current component magnitude can be minimized by skewing rotor slots. It can also be used to obtain motor speed. However, if the number of rotor bars is high, the component frequency range is wide making filtering difficult.

We can raise or lower the component magnitude by considering a special lamination design (Wolbank et al., 2002, 2003). However, the generalization is difficult since it is closely dependent upon many machine geometry parameters.

We do not neglect, in our study, the possible presence of saturation by taking into account the presence of the  $-\omega_c + h_i \omega_s$  components. We are studying the machine in a vector control scheme and, therefore, there is a main flux. This approach eliminates methods that work quite well in other studies (Degner and Lorenz, 1997 and Jansen, 1993).

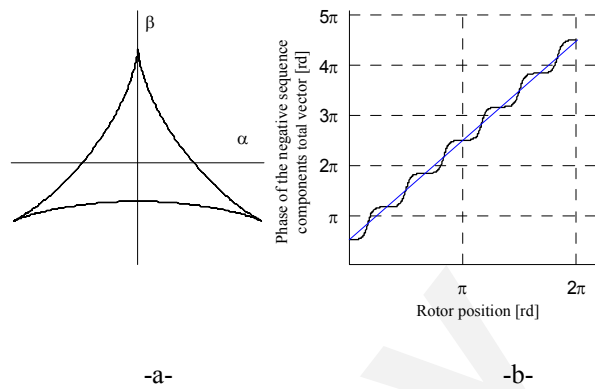


Fig. 3. -a- Theoretical negative sequence components locus representation in the  $-\omega_c$  reference frame, case of two saliencies ( $h_1=2, h_2=-4, \phi_1=\phi_2=0^\circ, I_{cn2}/I_{cn1}=0.5$ ).  
 -b- Phase of the negative sequence components total vector in respect to the rotor position.

Tracing the locus of the current components in the  $-\omega_c$  reference frame gives an idea of the multiple saliency configuration. A common case is the one represented in Fig. 3.a.

If we look closer at Fig. 3.b, we can notice that the relationship between the rotor position and the total vector phase is not a function in the mathematical meaning. Thus, for the same phase, we can have multiple positions. This depends on the saliency configuration. These figures are a necessary means to check which harmonics are present in the negative sequence current of the experimental machine (Fig. 10).

### 3. Synchronous Filtering

If we look at the current spectrum while performing the voltage carrier injection (Fig. 4), we will notice, in the case of two rotor speed dependent saliencies, negative sequence components near  $-\omega_c$ . This is an ideal result, as compared to what we mentioned above regarding the presence of asymmetries and saturation components.

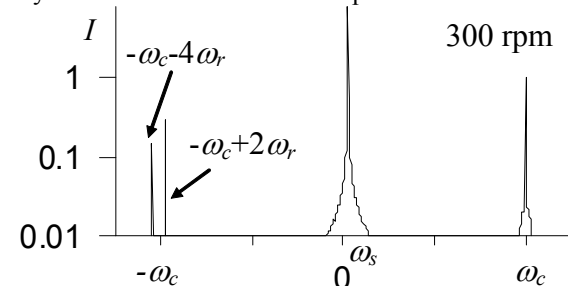


Fig. 4. Spectrum analysis of  $\alpha\beta$  stator current when a 400 Hz rotating voltage carrier is injected (simulation results).

To get rid of undesirable components and since we impose revolving carrier, we will use filters to extract negative sequence components. The study can be

handled in the frequency domain. We have multiple possibilities:

### 3.1 Analog and synchronous reference frame filters

We can, for example, use an analog band pass filter, which is centered on the carrier frequency. This will allow the elimination of the fundamental current component, PWM and high frequency, while keeping all the components that are close to  $\omega_c$  or  $-\omega_c$ . It has the advantage to allow the use of the full scale of the ADC for the carrier current components. Also, it does not require additional computing time like numerical filters. The problem is that such a filter may introduce an asymmetry that causes a negative sequence component which is not modulated by rotor position and other positive sequence components.

The remaining components will then be eliminated thanks to a synchronous frame high-pass filter (Fig. 5) (Teske et al. 2000a). This particular filter transforms the two  $\alpha\beta$  currents in a reference frame rotating at  $\omega_c$  and then a high pass filter is applied. Afterwards, the signal is switched back to the original reference frame. This synchronous filter eliminates near  $\omega_c$  components.

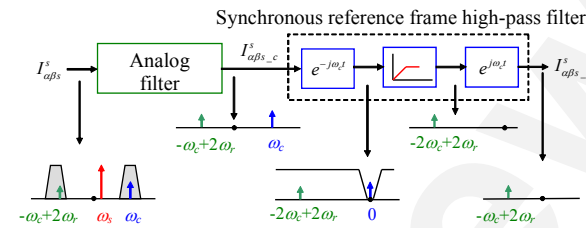


Fig. 5. Extracting negative sequence component using analog and synchronous frame high-pass filters.

### 3.2 Two successive synchronous reference frame filters

We can also use only synchronous reference frame filter to obtain the negative sequence components (Degner and Lorenz, 1997). This structure uses the previously presented feature of synchronous filters to eliminate the fundamental and the positive sequence in two separate steps (Fig. 6).

Bode diagram of this filter (Al-Rouh et al., 2003a) shows that the whole filter transfer-function gain is zero for the frequencies to be eliminated ( $\omega_s$  and  $\omega_c$ ) and equal to one for negative sequence components. The phase shift is also quasi null for these components. It appears that this is an ideal selective filter.

However, there are drawbacks: The time response of this structure is slow because of the use of first

order filters and the impossibility to eliminate perturbations near the  $-\omega_c$  components (Fig. 4). The latter disadvantage is common to many filtering structures studied because of the close spectral position in respect of the component looked for. Compensation schemes are then used to extract the only negative sequence we are interested in.

We also note the need for  $\omega_s$  to perform the first transformation. In a sensorless indirect rotor flux orientation control, the  $\omega_s$  will be generated thanks to the estimated speed, itself generated using the filter. This loop may lead to system instability.

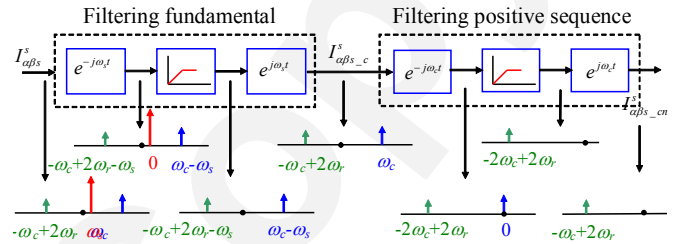


Fig. 6. Extracting negative sequence component using two successive synchronous frame filters.

### 3.3 Single low-pass synchronous frame filter

In this structure (Fig. 7), we use only one synchronous frame filter to get the negative sequence components (Al-Rouh et al., 2003a, 2003b). We first transform the  $\alpha\beta$  currents in a reference frame rotating at  $-\omega_c$ , then we keep only low frequency components and we switch back to the fixed stator reference frame.

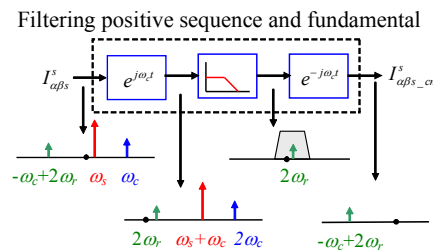


Fig. 7. Extracting negative sequence component using a single low-pass synchronous frame filter.

The simulation (Fig. 8 and Fig. 9) and experimental (Fig. 10 and Fig. 11) results are achieved using machine 1 (Appendix). This filter eliminates, in a single operation, the fundamental and positive sequence components. It does not rely on the knowledge of  $\omega_s$ , thus, it is independent from control operation. However, this filter introduces a phase shift in its band-pass. This shift can be estimated and does not affect speed estimation. The coefficient of this high order numeric filter must be chosen carefully in order to ensure system stability.

In Fig. 10, we roughly distinguish the previously simulated results of Fig. 3.a. and Fig. 8.

Fig. 11 indicates the magnitude of the current components and shows the effectiveness of the synchronous filter.

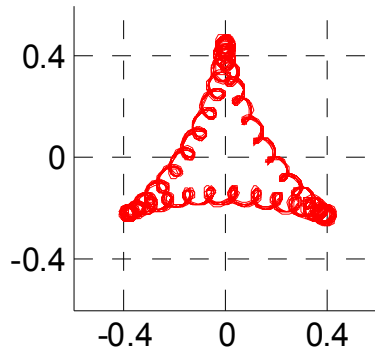


Fig. 8. Negative sequence components locus representation in the  $-\omega_c$  reference frame, case of two saliencies ( $h_1=2, h_2=-4, \phi_1=\phi_2=0^\circ, I_{cn2}/I_{cn1}=0.5$ ), simulation results on machine 1.

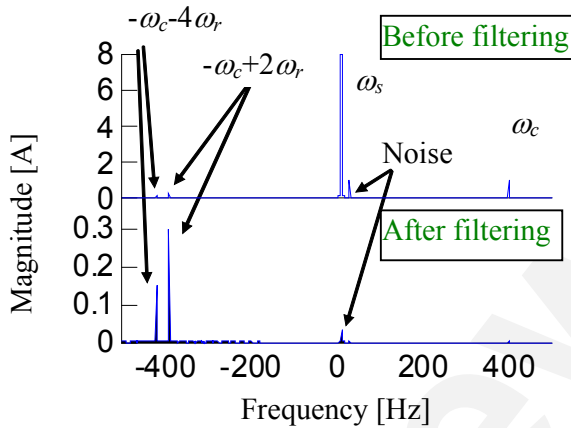


Fig. 9. Spectrum analysis of  $\alpha\beta$  simulated stator current with noise before and after the single low-pass synchronous frame filter.

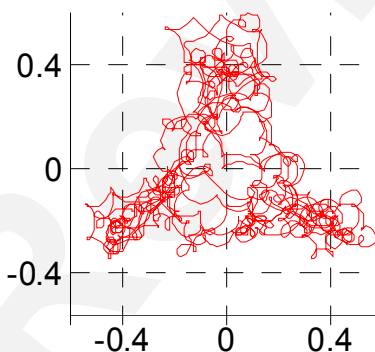


Fig. 10. Negative sequence components locus representation in the  $-\omega_c$  reference frame, case of two saliencies ( $h_1=2, h_2=-4, \phi_1=\phi_2=0^\circ, I_{cn2}/I_{cn1}=0.5$ ), experimental results on machine 1.

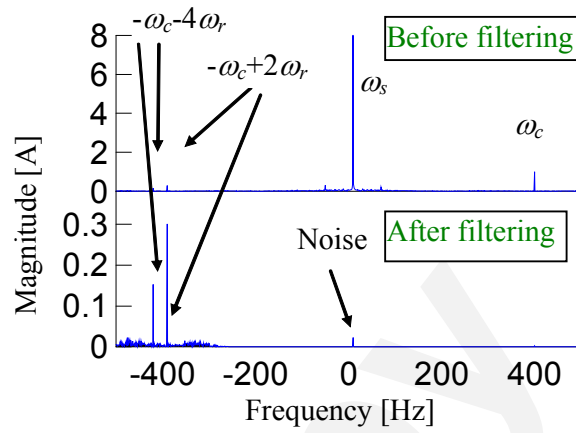


Fig. 11. Spectrum analysis of  $\alpha\beta$  experimental stator current before and after the single low-pass synchronous frame filter.

#### 4. Sliding discrete Fourier transform filtering

We present the formulation and theory of sliding discrete Fourier transform (SDFT) and then we apply it to filter the disturbing current components but also as a means to identify saliency characteristics.

##### 4.1 DFT theory

It is common to use, in such studies, the complex form of the discrete Fourier transform. Indeed, it differentiates between negative and positive frequencies, which represent negative and positive sequence components. We then have:

$$x[n] = \Re x[n] + j \Im x[n] \quad (6)$$

to represent the  $n^{\text{th}}$  sample of signal  $x$ , with :

$$\Re x[n] = x_\alpha[n] \text{ and } \Im x[n] = x_\beta[n] \quad (7)$$

The DFT formula is

$$X[k] = \sum_{n=0}^{N-1} x[n] e^{-j \frac{2\pi kn}{N}} = \Re X[k] + j \Im X[k] \quad (8)$$

with:  $-\frac{N}{2} \leq k \leq \frac{N}{2}$ . It uses  $N$  samples of the  $x$  signal to compute its discrete Fourier transform.

Let us show an example with the signal:

$$x(t) = A_m e^{j \frac{2\pi m}{NT_s} t} \quad (9)$$

with  $T_s$  the sampling period,  $N$  the number of samples. So, the signal frequency is:

$$\frac{m}{NT_s}$$

$$\text{The } n^{\text{th}} \text{ sample is: } x[n] = A_m e^{j \frac{2\pi mn}{N}} \quad (10)$$

$X[k]$  denotes the cross-correlation of the  $x(t)$  signal with a vector that is rotating at a frequency of

$k \frac{F_s}{N}$ , with  $F_s = \frac{1}{T_s}$  the sampling frequency.

$X[k] = N x[0]$  for  $k=m$ ,  $x[0] = A_m$  the signal magnitude.

$$X[k] = 0 \quad \text{for } k \neq m \quad (11)$$

The DFT allows us to get the magnitude and the phase of the vector at a particular frequency.

#### 4.2 SFDT theory

For real time running applications, where signals are being sampled and acquired synchronously every  $T_s$ , it is very interesting to use the sliding version of DFT.

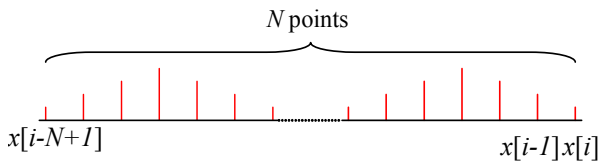


Fig. 12.  $N$  samples of  $x(t)$  signal.

We note  $x[i]$ , the signal at time  $iT_s$  (i.e. at the  $i^{\text{th}}$  sample). At this time, we have  $N$  samples ranging from the most recent  $x[i]$  to the most ancient  $x[i-N+1]$ .

We compute  $X_i[k]$  as defined above but for a frequency component  $k$  at the  $i^{\text{th}}$  sample.

$$X_i[k] = \sum_{n=0}^{N-1} x[i-n] e^{-j \frac{2\pi kn}{N}} \quad (12)$$

We also compute:

$$X_{i-1}[k] = \sum_{n=0}^{N-1} x[i-1-n] e^{-j \frac{2\pi kn}{N}} \quad (13)$$

With some arrangement, we get:

$$X_i[k] - X_{i-1}[k] e^{j \frac{2\pi k}{N}} = \frac{1}{N} (x[i] - x[i-N]) \quad (14)$$

This makes the computation of the DFT of any signal less time consuming, but it needs an "initialization" delay ( $N$  samples) to compute correctly the DFT. We will discuss the impact of this disadvantage later.

#### 4.3 Filtering and signal reconstruction

If we want to observe the signal in a limited frequency window, there is no need to compute

$X_i[k]$  for all the frequencies  $f = k \frac{F_s}{N}$ , but only in

the window  $[k_1, k_2]$  within  $\left[-\frac{N}{2}, \frac{N}{2}\right]$ .

Let us apply the SDFT to the current signal in the

stator reference frame  $I_{\alpha\beta}^s$ . By choosing a particular window around the component needed  $-\omega_c + 2\omega_r$ , and by reconstructing the signal in time domain, we obtain a filtered current in the stator reference frame that has neither a fundamental component nor a positive sequence one.

The inverse DFT leads to:

$$x[i-n] = \frac{1}{N} \sum_{k=k_1}^{k_2} X_i[k] e^{j \frac{2\pi kn}{N}} \quad (15)$$

For the  $i^{\text{th}}$  sample, the equation becomes simply a sum of the components magnitudes:

$$x[i] = \sum_{k=k_1}^{k_2} X_i[k] \quad (16)$$

So, the reconstruction is also less time consuming than it might be thought.

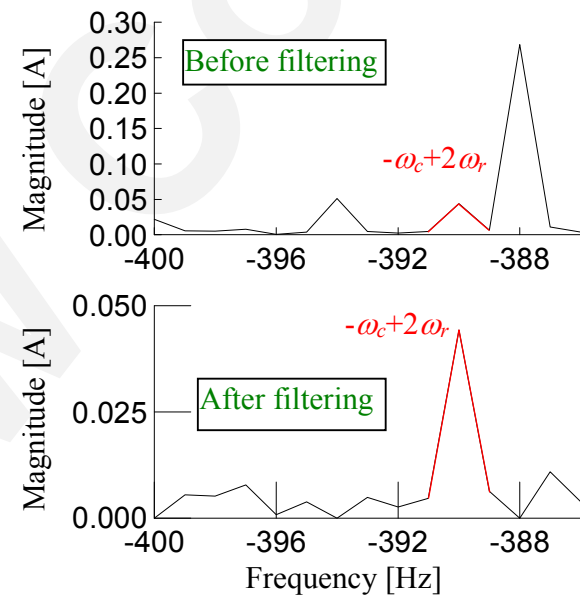


Fig. 13. Spectrum analysis of  $\alpha\beta$  experimental stator current before and after filtering with SDFT.

Fig. 13 shows the results of using this filter to the current of a loaded induction motor in speed control under IRFO (Indirect Rotor Filed Orientation). We use the SDFT to filter, not only off-band frequencies but also in-band specified ones, for example, the  $-\omega_c + 2\omega_s$  component. As we know its exact frequency, since we impose  $\omega_s$  thanks to the vector control scheme, we can easily eliminate it before reconstructing the current signal in time domain.

The advantage of this filter is the perfect filtering; it does not introduce any phase shift and it gives access to the frequency components individually. We can consider a machine with multiple saliencies as if it had only one saliency, the others being removed.

The major drawback of this filter is the initialization delay. For  $k_1=380$ ,  $k_2=420$ ,  $N=5000$ ,  $F_s=5$  kHz, the initialization delay is of 1 s. This delay can be shortened, by minimizing the number of samples  $N$ , but it induces a loss of resolution. So, a compromise that depends on the application has to be found. It has a serious impact on the control dynamics. The speed controller must be slowed down in order to ensure the system stability.

Filtering the current signal components, frequency by frequency, is possible thanks to SDFT filter if we know the magnitude to be subtracted from the spectrum data array. If two components overlap on a particular operating point, then, we can not force its magnitude to zero for filtering it. We must have identified the magnitude of the disturbing components in order to subtract it. This is the case with the  $-\omega_c + 2\omega_s$  and the  $-\omega_c + 2\omega_r$  components that cannot be distinguished at very low slip frequencies.

A possible solution is to track the component  $-\omega_c - 4\omega_r$  instead of  $-\omega_c + 2\omega_r$  to get rid of the  $-\omega_c + 2\omega_s$  problem at no load.

## 5. Rotor position tracking

This stage of the sensorless scheme is only possible when a full separation of negative sequence components is achieved. Two main techniques are discussed: Arctan function (Teske et al. 2000b) and phase locked loop (PLL) (Degner and Lorenz, 1997, Cilia et al., 1997 and Kim et al. 2002).

### 5.1 Arctan function

In the  $-\omega_c$  reference frame and with a single saliency, the negative sequence component is:

$$I_{\alpha\beta s_{-cn}}^{-\omega_c} = I_{cn} e^{j\left(h\theta_r + \frac{\pi}{2} + \varphi\right)} \quad (17)$$

We can extract the position using:

$$h\hat{\theta}_r + \varphi = \text{Arctan}\left(\frac{I_{\beta s_{-cn}}^{-f_c}}{I_{\alpha s_{-cn}}^{-f_c}}\right) - \frac{\pi}{2} \quad (18)$$

This method can be applied if there is only one saliency or if the other disturbing saliencies are of very low magnitude. The disturbing saliencies can also be filtered using SDFT filter for example. The important condition is that the signal to noise ratio must be high.

The advantage of such an estimator is its instantaneous response since it does not rely on a controller or loop scheme. Of course, the

implementation has to deal with the replacement of the traditional "atan2" function by a variant that uses increment of "arctan" to compute rotor position:

$$\Delta\hat{\theta}_r = \frac{1}{h} \Delta \text{Arctan}\left(\frac{I_{\beta s_{-cn}}^{-f_c}}{I_{\alpha s_{-cn}}^{-f_c}}\right) \quad (19)$$

$$\hat{\theta}_r[i] = \sum_{n=1}^{n=i} \Delta\hat{\theta}_r[n] \quad (20)$$

This will lead to the correct angle because of the  $1/h$  factor. The position that is obtained must be maintained in the  $[-\pi, \pi]$  range by a correct modulo-like function.

The results (Fig. 14) of a speed and position estimation shows that the algorithm gives correct results over a wide speed range.

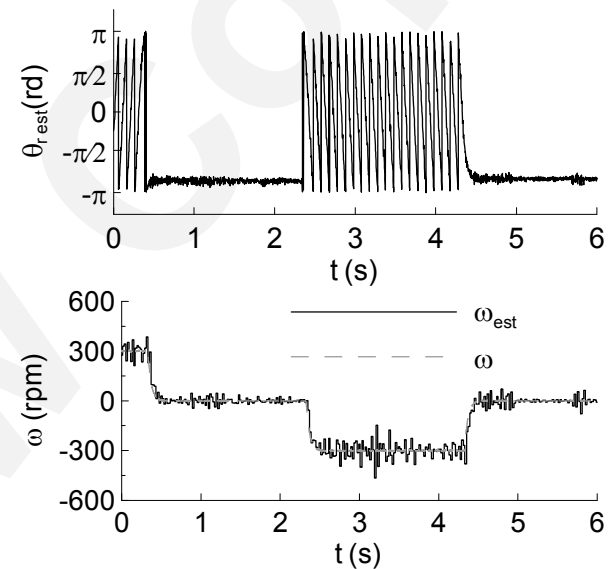


Fig. 14. Rotor speed and position estimation using Arctan function, experimental results of machine 1.

### 5.2 Phase Locked Loop

The PLL principle is the use of the  $I_{\alpha\beta s_{-cn}}^{-\omega_c}$  experimental current components and the ones issue from a saliency model, to compute a variation (or increments) of  $\hat{\theta}_r$  and then angle itself. It forms a tracking observer (Degner and Lorenz, 1997).

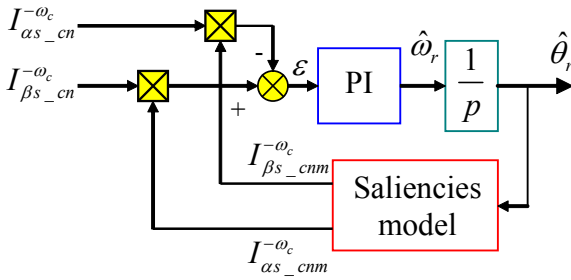


Fig. 15. Rotor speed and position estimation using a PLL.

The saliency model is more or less complex in order to take into account the disturbing current components  $(-\omega_c + 2\omega_r, -\omega_c + 2\omega_s, -\omega_c, -\omega_c + \frac{N}{p}\omega_r)$  involving saturation, estimation or commissioning (Teske et al. 2000a). The error is:

$$\varepsilon = I_{\alpha s\_cnm}^{-\omega_c} I_{\beta s\_cn}^{-\omega_c} - I_{\alpha s\_cn}^{-\omega_c} I_{\beta s\_cnm}^{-\omega_c} \quad (21)$$

$\varepsilon \rightarrow 0$  when  $\hat{\theta}_r \rightarrow \theta_r + \frac{\varphi - \hat{\varphi}}{h}$ , the last terms are time independent.

In the case of non-modeled multi-saliency, the algorithm will estimate the position of the resulting vector  $\bar{I}_{cn1} + \bar{I}_{cn2}$  (Fig. 16).

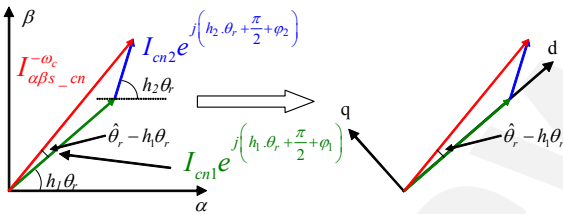


Fig. 16. Position estimation error due to a non-modeled saliency.

Maximum error is reached if the components are of the same magnitude.

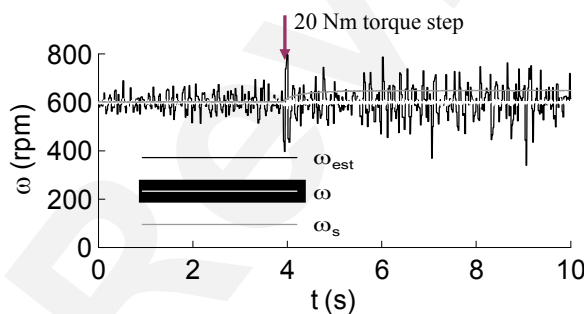


Fig. 17. Rotor speed estimation using a PLL, experimental results.

We hardly notice, on Fig. 17, that when a load of 20 Nm is applied at  $t = 4$  s, the  $\omega_s$  increases. The real speed  $\omega_r$  and the estimated speed  $\hat{\omega}_r$  remain constant because of the speed control in an IRFO scheme. We also note the high frequency oscillations

around the mean value of  $\hat{\omega}_r$ , due to noise on the negative sequence component of the PLL inputs.

## 6. Identification of model parameters

As already seen, the PLL requires the knowledge of the magnitude and phase of the negative sequence components in order to achieve rotor position tracking. We must also identify other components, if they exist, for introducing a compensating model. We studied two methods that we will discuss: The least square algorithm, that can be carried off-line and, an original method, which we called "synchronization algorithm". Its identification process is based on DFT and can be performed online.

### 6.1 Least square algorithm (LSA)

The formulation we propose is as follows. Let us take a multi-saliency model where:

$$I_{\alpha\beta s\_cn}^{-\omega_c} = \sum_{i=1}^{N_C} I_{cni} e^{j(h_i \theta_r + \frac{\pi}{2} + \varphi_i)} \quad (22)$$

With  $N_C$ , the number of components to be identified.

As the function is non-linear, due to the presence of trigonometric functions, we must find auxiliary parameters  $\xi_i$  to identify (23). After identification, we compute the original parameters.

$$I_{\alpha\beta s\_cn}^{-\omega_c} = \sum_{i=1}^{N_C} \xi_i e^{jh_i \theta_r} \quad \text{with} \quad \xi_i = I_{cni} e^{j(\varphi_i + \frac{\pi}{2})} \quad (23)$$

We form the input "X" and output "Y" vectors of  $N$  samples:

$$\begin{bmatrix} y_1 \\ \vdots \\ y_N \end{bmatrix} = \begin{bmatrix} \psi_1(x_1) & \cdots & \psi_{N_C}(x_1) \\ \vdots & \ddots & \vdots \\ \psi_1(x_N) & \cdots & \psi_{N_C}(x_N) \end{bmatrix} \begin{bmatrix} \xi_1 \\ \vdots \\ \xi_{N_C} \end{bmatrix} \quad (24)$$

The cost criterion is:

$$J = \frac{1}{2} \sum_{n=1}^N \left( y_n - \sum_{i=1}^{N_C} \psi_i(x_n) \cdot \hat{\xi}_i \right)^2 \quad (25)$$

The LSA gives the parameters as:

$$\hat{\Xi} = \begin{bmatrix} \hat{\xi}_1 & \cdots & \hat{\xi}_{N_C} \end{bmatrix}^t = (\psi^t \psi)^{-1} \psi^t Y \quad (26)$$

In our case:

$$X = [\theta_1 \quad \cdots \quad \theta_N]^t \quad (27)$$

$$Y = \begin{bmatrix} I_{\alpha\beta s\_cn1}^{-\omega_c} & \cdots & I_{\alpha\beta s\_cnN}^{-\omega_c} \end{bmatrix}^t \quad (28)$$

So

$x_n = \theta_{r,n}$  is the position at the  $n^{th}$  sample

$y_n = I_{\alpha\beta s\_cn}^{-\omega_c}$  is the current component, in the carrier rotating reference frame, at the same sample

The  $\Psi$  matrix is given by:

$$\Psi = \left[ e^{jh_i\theta_m} \right] \text{ for } i = \overline{1, N_C} \text{ and } n = \overline{1, N} \quad (29)$$

After calculating the optimum parameters  $\hat{\xi}_i$  we deduce:

$$\hat{I}_{cni} = \sqrt{\hat{\xi}_{\alpha i}^2 + \hat{\xi}_{\beta i}^2} \quad (30)$$

$$\hat{\phi}_i = \text{Arc tan} \left( \frac{\hat{\xi}_{\beta i}}{\hat{\xi}_{\alpha i}} \right) - \frac{\pi}{2} \quad (31)$$

The computation process in order to compute  $\hat{\Xi}$  is heavy and should be carried off-line. We must have the whole data set, including rotor positions, to use the LSA. The experimental results using machine 1 are shown on Fig. 18.  $\hat{I}_{\alpha s\_cn}^{-\omega_c}$  and  $\hat{I}_{\beta s\_cn}^{-\omega_c}$  are computed after the identification process of the model parameters and they are compared with the real current components. They evidence the effectiveness of the LSA in the identification of saliency model parameters.

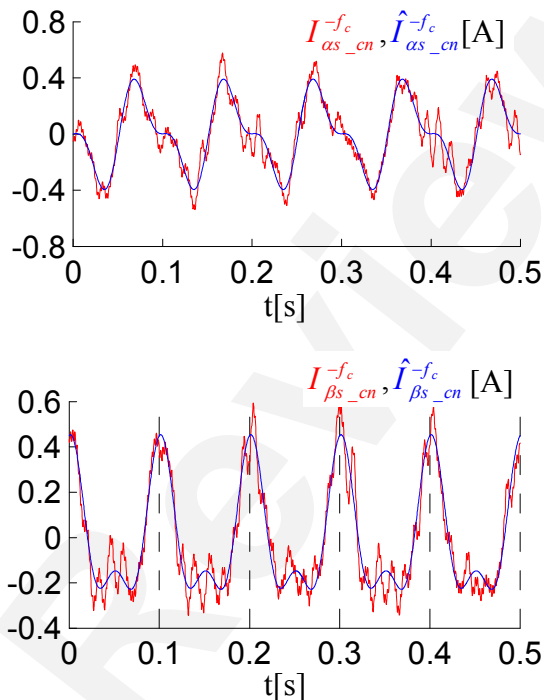


Fig. 18. Negative sequence components after estimation.

### 6.2 Synchronization algorithm

We named the method this way because of the principle use of a transformation to a particular reference frame "synchronized" with the one of the

harmonic component we want to identify.

Assume we have the same model as (22).  $I_{cni}$  and  $\phi_i$  are the parameters we are looking for. When we transform the measured current from carrier rotating frame into the reference that is synchronized with the harmonic  $h_m$ , the expression becomes:

$$I_{\alpha\beta s\_cn}^{-\omega_c} e^{-jh_m\theta_r} = \sum_{i=1}^{N_c} I_{cni} e^{j\left(\phi_i + \frac{\pi}{2}\right)} e^{j(h_i\theta_r - h_m\theta_r)} \quad (32)$$

Then, we sum over one  $\theta_r$  revolution period:

$$\text{Sum} = \int_0^{2\pi} I_{\alpha\beta s\_cn}^{-\omega_c} e^{-jh_m\theta_r} d\theta_r \quad (33)$$

only the term with  $h_i = h_m$  will remain:

$$\text{Sum} = 2\pi I_{cni} e^{j\left(\phi_i + \frac{\pi}{2}\right)} \quad (34)$$

The same consideration applies to a discrete version of the algorithm where we must divide by the number of samples, thus, meeting the definition of DFT.

Three conditions must be met to guarantee the correctness of the results: the respect of Shannon theorem, the spectral difference between two components must be larger than DFT resolution and that, over the samples; we must have an integer number of rotor turns.

An identification example is shown on Fig. 19. The process is carried online on the DSP board (Appendix). The magnitude is well identified after the initialization delay of the algorithm. The variation of this magnitude can also be monitored for parameter adaptation or for diagnosis purposes.

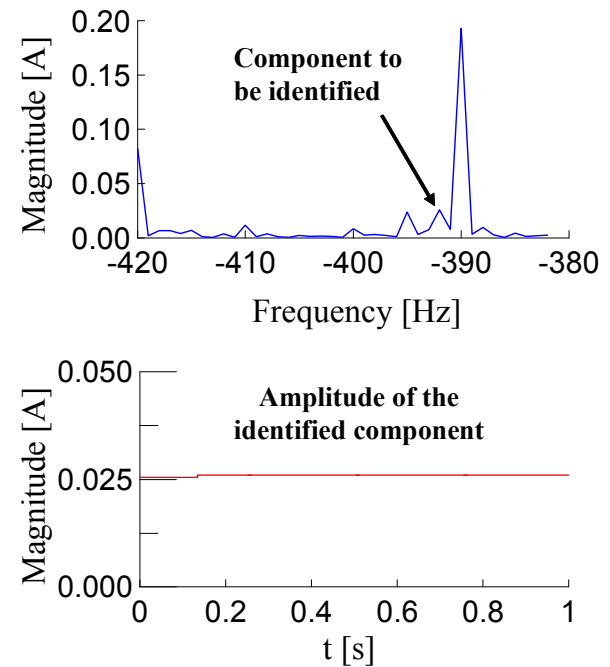


Fig. 19. Spectral analysis of the negative sequence component current, showing the identified components and its magnitude after process.

**7. Estimation et control**

We present the results of machine 1 under indirect vector rotor field orientation. The estimated speed is used in the control scheme, both for computing Park transformation angle and for the speed controller. The case of single and multi saliency are shown on Fig. 20 and Fig. 21 with the PLL method. We observe that the estimator is stable with a relative numerical noise magnitude.

The lag introduced in the speed estimation signal is due to a numerical filter we were obliged to apply in order to get smoother speed estimation. As one can notice, there is a lot of noise on speed estimation, at the output of the PI controller (PLL method) or on the derivative of the angular position (Arctg method).

Fig. 22 and Fig. 23 show the experimental results when full sensorless closed loop is applied for booth speed estimation for vector control and for speed controller input. Only PLL results are presented since the SDFT estimator has a relatively long initialization time and did not give satisfactory results in closed loop operation.

Standstill operation (Fig. 22) and low speed with sudden load (Fig. 23 and Fig. 24) are presented. Vector control is well achieved;  $I_{ds}$  and  $I_{qs}$  currents are not disturbing each other during the transients. The Standstill load (Fig. 22) is low because of the means used (hand load applied). We have a powder brake that can only apply  $T_r = a \cdot \Omega_r$  torque type.

When a 20 Nm load torque is applied at 6 rpm (Fig. 23 and Fig. 24), the speed lowers, then recovers its reference value. We observed that the disturbance rejection is faster when Arctan estimator is used because of its instantaneous response in comparison with the PLL estimator. The estimated speed is however noisy and leads to some noise on the  $I_{qs}$  reference current because of the computed slip frequency in IRFO.

The noise is due to the way the estimated speed is computed thanks to the PI controller of the PLL structure. We can notice that the estimated angle  $\theta_{r\ est}$  does not change between -0.5 to 1.5 s, and is nearly equal to  $\pi$ . In this period, the machine stops because of the sudden load, then the disturbance is rejected and the machine rotates again at 6 rpm.

We added (Fig. 22) a comparison with a sensed vector control while applying a sudden load of 20 Nm when the machine is at low speed (6 rpm). The

speed time response is 2 s in both cases because of the speed controller parameters. In fact, we were obliged to slow down the controller to avoid nasty oscillations due to high noise on the estimated speed and to the internal lag.

If we fine tune the speed controller with a sensed vector control on the same machine, then the load disturbance rejection is made in less than 0.8 s.

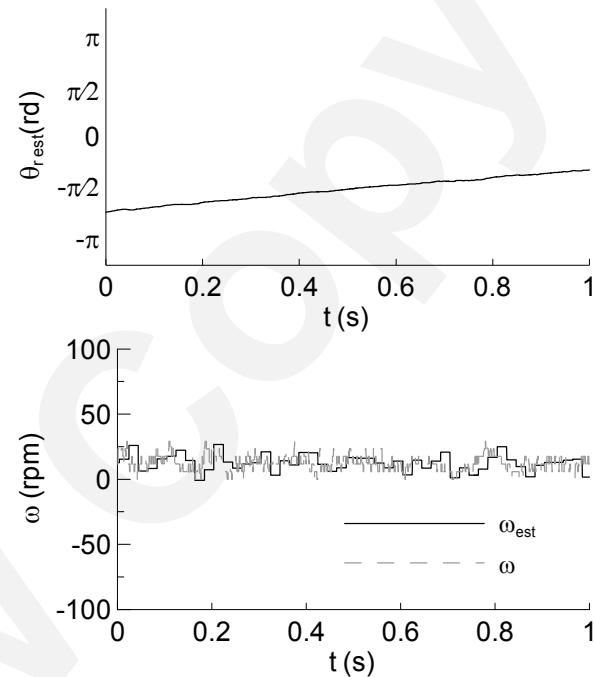


Fig. 20. Estimation of speed and position by PLL for one saliency machine at 6 rpm under vector control.

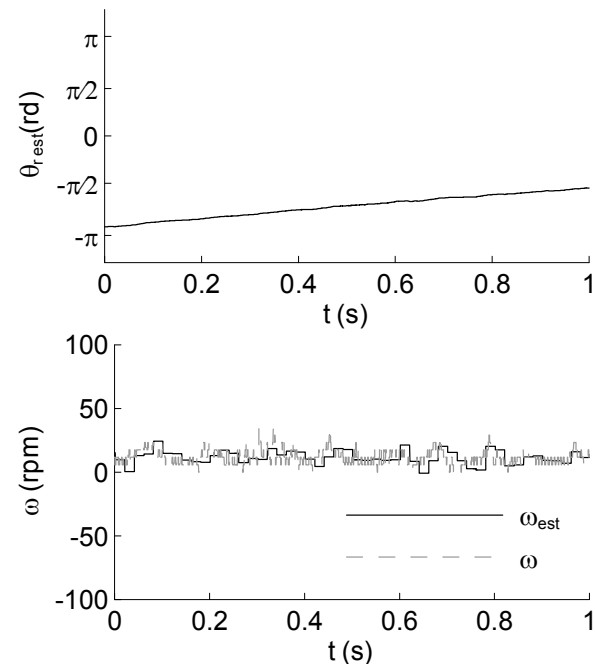


Fig. 21. Estimation of speed and position by PLL for multy saliencies machine at 6 rpm under vector control.

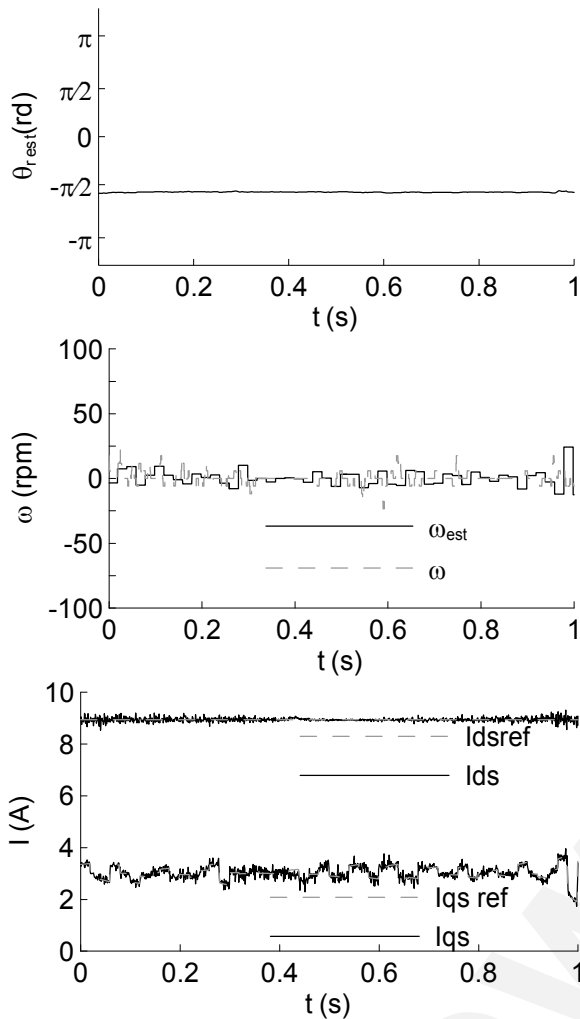


Fig. 22. Estimation of speed and position by PLL for one saliency machine under sensorless vector control at standstill under load.

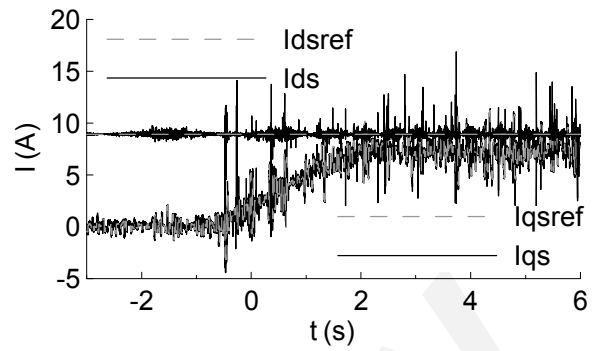
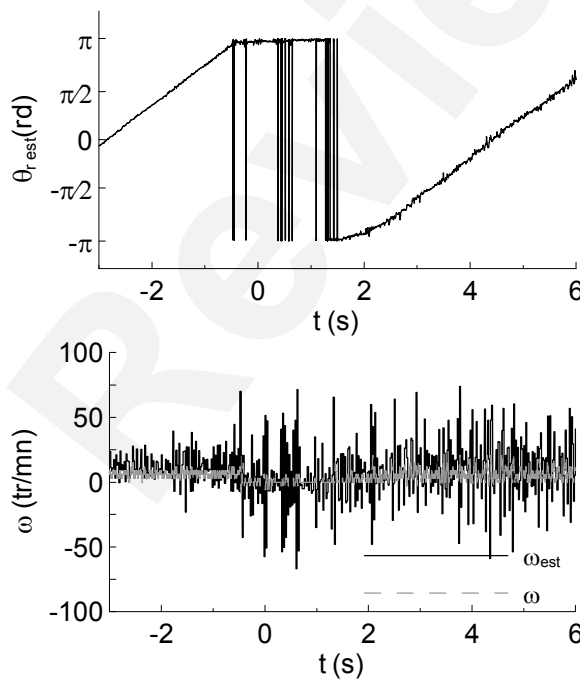


Fig. 23. Estimation of speed and position by PLL for one saliency machine at 6 rpm under sensorless vector control, sudden application of 20 Nm load.

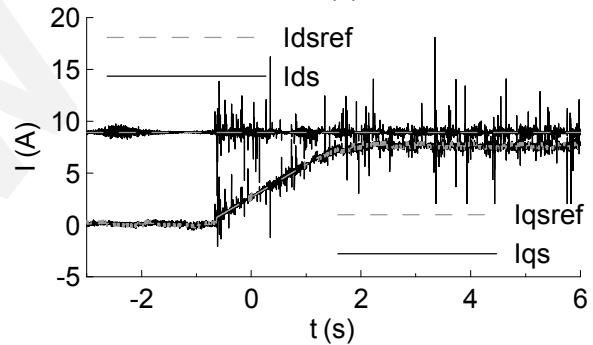
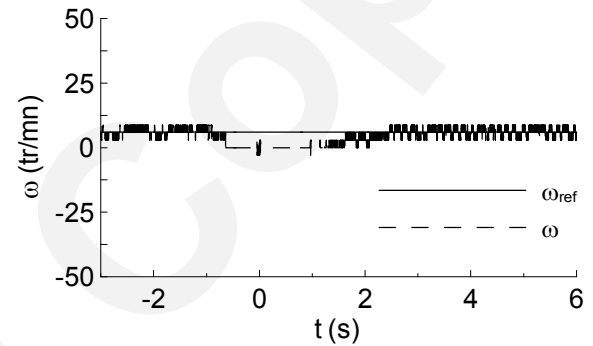


Fig. 24. Comparison with a full sensed vector control, at 6 rpm, sudden application of 20 Nm load.

### 8. Conclusion

This paper presents the necessary methods to achieve speed estimation in a sensorless vector control scheme (IRFO). Many filtering and parameter identification aspects are discussed. The results were carried on a particular machine that helped us to model the saliencies in order to study the behaviour of the filters and estimators.

We also implemented these methods on machines with particular rotor saliencies (small permanent magnet glued on the end ring, motor with a broken bar, peripheral milling on the rotor laminations). Unfortunately, the saliency level was low regarding machine geometry.

We aim at going further in this research subject to find the best saliency scheme in order to get a higher signal to noise magnitude while minimizing torque disturbance under vector control.

This can only be achieved with engineered rotors and special saliency configuration.

Another aspect is the commissioning which is unique to each motor. There are important disturbances due to saturation and load influence on the negative sequence current components. An auto-identification and diagnosis algorithm must be developed to allow the portability of the sensorless control on different machines with minimum tuning.

## Appendix

### Machine 1

The results presented in this paper are those obtained with a 5.5 kW induction motor, named machine 1, it is a 2-pair pole machine with no saliencies. We also carried studies on other 3 kW machines with modified rotors. Machine 1 operates under vector control. For the sake of the study, we added a saliency model implemented in the DSP control program that takes, as an input, the rotor position measured with a 4096 points incremental encoder and gives, as an output, the current with carrier components, as if they were generated by a machine with saliency.

These components are added to the real currents (in stator fixed frame) and are entered into the control and estimator algorithm.

We worked on many possible saliency configurations (number and magnitude of saliencies), but we present results on machine 1 with one saliency ( $h_1=2$ ) and two (multi) saliencies ( $h_1=2$ ,  $h_2=4$ ) (fig. 8). These configurations were found on experimental machines.

This approach allows us to easily test the algorithms developed for different saliency configurations and study the effectiveness of the estimation algorithms.

### Control board

The program is run on a 250 MHz PowerPC DSP of the DS1104 dSPACE board. The 10 kHz PWM is performed with the slave TMS320F240 DSP within the same card. The algorithms are programmed in C high level language to make them comparable with the simulation process developed. In order to achieve optimal coding of the algorithms in terms of real time processing, we did not use Simulink code generation tool.

The current loop sampling period is 200  $\mu$ s and the speed one is 1 ms. The vector control is a classical indirect rotor field orientation (IRFO). The voltage fed inverter uses IGBT with low dead band delays. The injection frequency is of 400 Hz.

Considering the execution time, we observe 67  $\mu$ s for the execution of the SDFT and filtering algorithms. The two successive synchronous reference frame filters require 7  $\mu$ s whereas the single low-pass synchronous frame filter takes 5.2  $\mu$ s. The speed estimation using PLL with the synchronous filter takes place in 33  $\mu$ s. These algorithms are executed within the 200  $\mu$ s vector control loop.

## References

- Al-Rouh I, Baghli L, Rezzoug A. (2003a). Modelling multiple saliencies in rotor-faulty induction machine for rotor position estimation. *Proceeding of the 10<sup>th</sup> European Power Electronics (EPE) Conf.* 2 - 4 Sept. paper 0414.pdf. pp.1 - 10, Toulouse, France.
- Al-Rouh I, Baghli L, Rezzoug A. (2003b). Estimation de la position de la machine asynchrone. *Proceeding of Electrotechnique du Futur.* 9 - 10 Dec. paper 15-alrouh\_ef2003.pdf, pp. 1 - 5, Gif sur Yvette, France.
- Blaschke F, Van der Burgt J, Vandemput A. (1996). Sensorless direct field orientation at zero flux frequency. *Conf. Rec. IEEE-IAS Annual Meeting.* n°31, vol. 1. pp. 189 - 196, San Diego, USA.
- Cilia J, Asher GM, Sumner M, Bradley KJ. (1997). Sensorless position detection for vector-controlled induction motor drives using an asymmetric outer-section cage. *IEEE Transactions on Industry Applications.* vol. 33. n°5. Sept./Oct. pp. 1162 - 1169
- Consoli A, Testa A. (2003). An alternative to high frequency current detection techniques for zero speed sensorless control of AC motor drives. *EPE Journal.* vol. 13. n°3, Aug. pp. 30-31.
- Degner MW, Lorenz RD. (1997). Using multiple saliencies for the estimation of flux, position, and velocity in AC machines, *Proceeding of IEEE-IAS 1997 Annual Meeting.* vol. 1. 5 - 9 Oct. pp. 760 - 767.
- Ha JI, Sul SK. (1997). Sensorless field orientation control of an induction machine by high frequency signal injection. *Proceeding of IEEE-IAS 1997 Annual Meeting.* vol. 1. 5 - 9 Oct. pp. 426 - 432.
- Holtz, J. (2002). Sensorless control of induction motor drives, *Proceedings of the IEEE.* vol. 99. n°8. Aug. pp. 1359-1394. [Online]. Available: <http://www.ema.uni-wuppertal.de/paper/sensles.pdf>.
- Holtz, J. (1998). Sensorless Position Control of Induction Motors - An Emerging Technology, *IEEE Transactions on Industrial Electronics.* vol. 45, n°6. Dec. pp. 840 - 852.
- Jansen PL. (1993). The integration of state estimation, control, and design for induction machine. PhD thesis. Department of Electrical and Computer Engineering. University of Wisconsin, Madison.
- Kim H, Harke MC, Lorenz RD. (2002). Sensorless control of interior permanent magnet machine drives with zero-phase-lag position estimation. *Conf. Rec. IEEE-IAS.* n°31. paper 43P2.pdf, Pittsburgh, USA.
- Schroedel M. (1996). Sensorless control of AC machines at low speed and standstill based on the INFORM method. *Proceeding of IEEE-IAS 1996 Annual Meeting.* vol. 1. 6 - 10 Oct. pp. 270 - 277.

- Staines CS, Asher GM, Bradley KJ. (1999). A periodic burst injection method for deriving rotor position in saturated cage-salient induction motors without a shaft encoder. *IEEE Transactions on Industry Applications*. vol. 35. n°4. July/Aug. pp. 851 - 858
- Teske N, Asher GM, Sumner M, Bradley KJ. (2000a). Suppression of saturation saliency effects for the sensorless position control of induction motor drives under loaded conditions. *IEEE Transactions on Industrial Electronics*. vol. 47. n°5. Sep./Oct. pp. 1142 – 1150.
- Teske N, Asher GM, Sumner M, Bradley KJ. (2000b). Sensorless position estimation for symmetric cage induction motor under loaded conditions. *Proceeding of IEEE Industry Applications Conference*. vol. 3. 8 - 12 Oct. pp. 1835 – 1841.
- Wolbank TM, Woehrschimmel R, Machl JL. (2002) Zero speed sensorless control signals of induction motors with closed rotor slots. *Proceeding of IEEE Power Electronic Specialists Conference, PESC 02*. vol. 2. 23 - 27 June. pp. 997 – 1002
- Wolbank TM, Woehrschimmel R, Machl JL. (2003). Lamination design variations for improved performance of zero speed sensorless controlled induction machines, *EPE Journal*. vol. 13. n°3. Aug. pp. 36–42.

Review Copy